AD

AD-E404 222

Technical Report ARMET-TR-18051

WRAPAROUND ANTENNA FOR S-BAND TELEMETRY

Aaron Barton

July 2020

U.S. ARMY COMBAT CAPABILITIES DEVELOPMENT COMMAND ARMAMENTS CENTER

Munitions Engineering Technology Center

Picatinny Arsenal, New Jersey

The views, opinions, and/or findings contained in this report are those of the author(s) and should not be construed as an official Department of the Army position, policy, or decision, unless so designated by other documentation.

The citation in this report of the names of commercial firms or commercially available products or services does not constitute official endorsement by or approval of the U.S. Government.

Destroy by any means possible to prevent disclosure of contents or reconstruction of the document. Do not return to the originator.

REPORT DOCUMENTATION PAGE		*Form Approved* *OMB No. 0704-01-0188*

The public reporting burden for this collection of information is estimated to average 1 hour per response, including the time for reviewing instructions, searching existing data sources, gathering and maintaining the data needed, and completing and reviewing the collection of information. Send comments regarding this burden estimate or any other aspect of this collection of information, including suggestions for reducing the burden to Department of Defense, Washington Headquarters Services Directorate for Information Operations and Reports (0704-0188), 1215 Jefferson Davis Highway, Suite 1204, Arlington, VA 22202-4302. Respondents should be aware that notwithstanding any other provision of law, no person shall be subject to any penalty for failing to comply with a collection of information if it does not display a currently valid OMB control number.
PLEASE DO NOT RETURN YOUR FORM TO THE ABOVE ADDRESS.

1. REPORT DATE (DD-MM-YYYY) July 2020	2. REPORT TYPE Final	3. DATES COVERED (*From - To*) January 2017 to June 2018

4. TITLE AND SUBTITLE Wraparound Antenna for S-band Telemetry	5a. CONTRACT NUMBER
	5b. GRANT NUMBER
	5c. PROGRAM ELEMENT NUMBER
6. AUTHORS Aaron Barton	5d. PROJECT NUMBER
	5e. TASK NUMBER
	5f. WORK UNIT NUMBER

7. PERFORMING ORGANIZATION NAME(S) AND ADDRESS(ES) U.S. Army CCDC AC, METC Fuze and Precision Armaments Directorate (FCDD-ACM-FI) Picatinny Arsenal, NJ 07806-5000	8. PERFORMING ORGANIZATION REPORT NUMBER

9. SPONSORING/MONITORING AGENCY NAME(S) AND ADDRESS(ES) U.S. Army CCDC AC, ESIC Knowledge & Process Management Office (FCDD-ACE-K) Picatinny Arsenal, NJ 07806-5000	10. SPONSOR/MONITOR'S ACRONYM(S)
	11. SPONSOR/MONITOR'S REPORT NUMBER(S) Technical Report ARMET-TR-18051

12. DISTRIBUTION/AVAILABILITY STATEMENT

Approved for public release; distribution is unlimited.

13. SUPPLEMENTARY NOTES

14. ABSTRACT

   This report summarizes a wraparound conformal antenna for use in smart munitions and S-band telemetry. It uses quarter-wavelength patch radiating elements and has been tested on 155-mm artillery platforms with success. The antenna is small, inexpensive to produce, and requires no external matching components. Simulations and measurements of the return loss and radiation pattern are given with the antenna mounted on a Precision Guidance Kit shaped fuze and an M483A1 projectile. Analytical models of the antenna that predict the radiation pattern are also given.

15. SUBJECT TERMS

Telemetry   Wireless   High-g   Gun-launched   DFuze   Aerofuze   Antennas   Wraparound   Conformal antenna   Quarter-wavelength patch   Cavity-back slot

16. SECURITY CLASSIFICATION OF:			17. LIMITATION OF ABSTRACT	18. NUMBER OF PAGES	19a. NAME OF RESPONSIBLE PERSON Aaron E. Barton
a. REPORT U	b. ABSTRACT U	c. THIS PAGE U	SAR	41	19b. TELEPHONE NUMBER (Include area code)

Standard Form 298 (Rev. 8/98)
Prescribed by ANSI Std. Z39.18

CONTENTS

FIGURES

FIGURES
(continued)

ACKNOWLEDGMENTS

INTRODUCTION

Wraparound antennas are a popular option for large caliber smart projectiles requiring radio services, where the nosecone is otherwise unavailable for antenna placement. These antennas typically consist of an array of microstrip radiating elements, fed by a microstrip or stripline power division network, and fabricated on a flexible substrate that is bent to conform to the projectile's outer surface. These antennas are then flush-mounted to the projectile so as to not aerodynamically disturb the airframe shape. The goal for most wraparound antennas is to use an array of radiating elements along the outer circumference of the projectile that, when combined with the ground-plane effects of the projectile chassis, yields a radiation pattern with minimum variation in the roll plane as possible. This avoids having to place an antenna at the projectile nose (ref. 1). The array needs to be driven with a feed network that appropriately phases each radiating element. This feeding network usually integrated into the substrate of the antenna itself out of convenience, allowing the entire array to be driven with only a single master feed from a radio frequency (RF) transmitter. This is in contrast to developing the array from individual antennas mounted on the outside of the projectile, where the feed network would need to be included within the electronics of the smart munition (refs. 2 through 4).

This report describes a wraparound antenna, which uses two side-fed, quarter-wavelength patch elements fabricated over an edge-plated and rear-plated polytetrafluoroethylene (PTFE) substrate for typical use with 1 to 3-in. diameter fuze sections of a smart projectile. A two-dimensional sketch of the wraparound artwork is seen in figure 1. The geometry can be altered to work with other diameters and operating frequencies. The antenna is fabricated from a single-layer Teflon™ microwave substrate with copper-cladding on both sides. It is nominally tuned for use in S-band telemetry, but it can be tuned for other radio services by changing the dimensions of the patch elements, notably their vertical lengths.

A   B
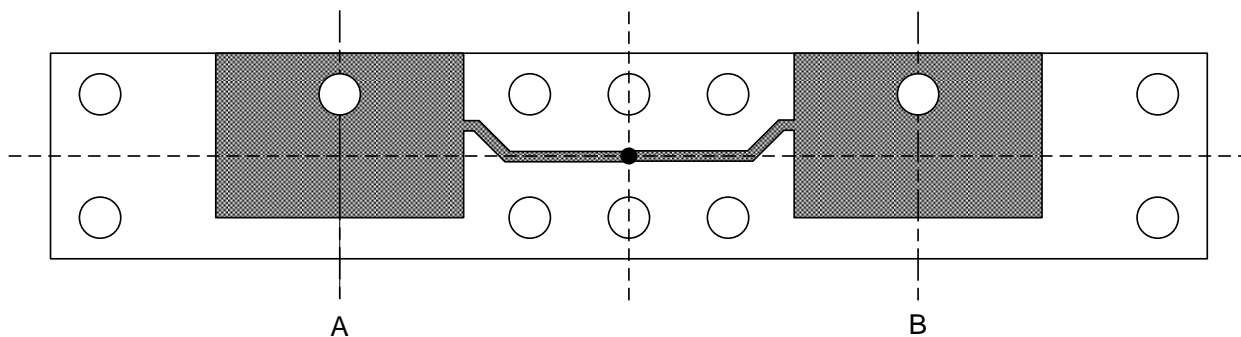
Figure 1
Wraparound antenna described in this report

Wraparound antennas for missiles and smart munitions trace their origins to conformal microstrip and cavity-backed slot designs from the 1970s (refs. 5 through 9) with early concepts from the 1950s (refs. 10 through 13). Development on these types of projectile antennas occurred concurrently with other types of designs, including dielectric-filled edge-slot (refs. 14 and 15) and slotted waveguide antennas (ref. 16). Companies, such as Ball Aerospace, Boulder, CO, and Haigh-Farr Inc., Bedford, NH, and organizations, such as the former Harry Diamond Laboratories (currently U.S. Army Adelphi Research Laboratories, Adelphi, MD), have been industry leaders in this area.

Improvements over the decades to conformal microstrip designs have included adding multiple radiating elements to support multiple radio services and integrating RF filters into the conformal substrate. Modern features (such as u-slots and notches) to the radiating elements have been added to support circular polarization, broad-band operation, multi-band operation, or to

suppress unwanted radiation (refs. 10, 17, 18, and 19). These have followed trends in microstrip patch antenna technologies (ref. 20) for other applications including consumer electronics.

The behavior of a conformal patch or cavity backed slot element can be estimated analytically by the cylindrical cavity model (refs. 21 through 23) where the interior of the patch is treated as a cylindrical cavity with electric walls on its upper and lower surfaces and magnetic walls on its edges. The fields are solved on the magnetic walls, which then are treated as apertures radiating from an infinite-length cylinder representing the projectile body. Behavior can also be estimated analytically using the surface-current model (refs. 24 and 25) where the surface current on the patch element (rather than the fields at its edges) is treated as radiating over an infinite-length cylinder with a dielectric substrate and optional superstrate. Geometrical theory of diffraction (ref. 26) can be further used to refine the estimates for finite-length cylinders, which describes the actual radiation pattern from a real finite-length projectile.

ANTENNA DESIGN AND FABRICATION

The designed wraparound antenna is show in figure 2 as a three-dimensional (3D) computer-aided design (CAD) model. The antenna was designed using combination of electronic CAD, mechanical CAD, and computational electromagnetic tools. This included ANSYS Electronics Desktop 2018 [also regarded in industry as Ansoft high frequency structural simulator (HFSS)], PTC CREO, and Altium Designer. Multiple iterations were performed virtually with the most promising versions sent for printed circuit board fabrication. Fabricated iterations were mounted on representative projectile housings and measured for performance. This process was then repeated.
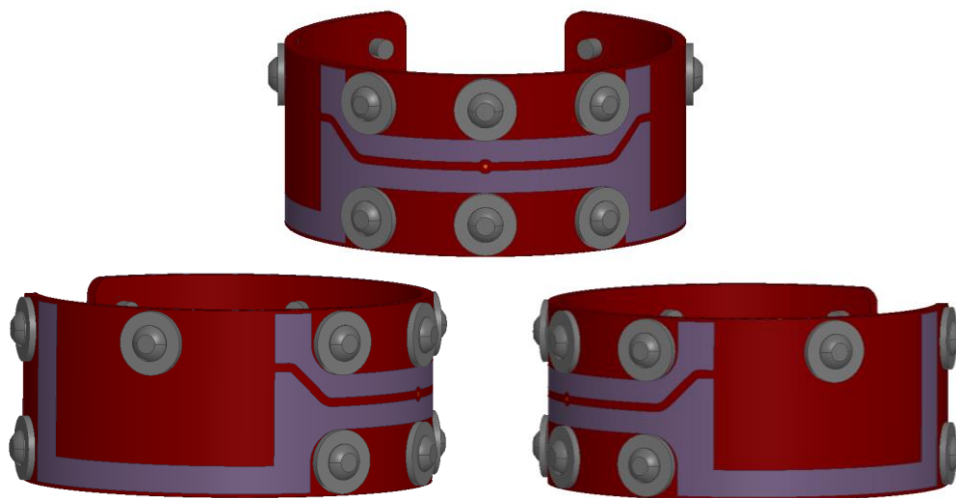
Figure 2
Designed wraparound antenna (front-view, left-view, right-view)

The design consists of two quarter-wavelength microstrip elements, fabricated on a single-layer, edge-plated strip of copper-clad Rogers RT/duroid 5870 PTFE substrate [0.062 in. in thickness and relative dielectric constant (dk) of 2.33]. The antenna is formed by bending it around the circumference of a section of the projectile fuze, and it sits in a 1.1-in. tall, 0.070-in. deep pocket. All of the edges of the substrate have been plated in order to reduce the detuning effect when the antenna is situated within the metal pocket on the fuze housing (ref. 27). Twelve plated mounting holes have been included for fastening with additional metal plating around the holes for strength. Two of the mounting holes are directly through the patches near the upper plating, providing even

coverage by the bolting patterning. The patch elements have been tuned to include the effects of these holes.

The patch elements are placed on the substrate so that they fall diametrically opposite each other when the antenna is seated around the projectile. Each patch is side-fed from a pair of 100-ohm microstrip traces, which join together at a T-junction feed with a centrally located 50-ohm coaxial cable. The feeding position with each patch element is placed vertically along the elements for the best impedance match (i.e., the 100-ohm point). The microstrip traces are bent to meet with the patch at this location. Pertinent dimensions of the antenna traces and patch elements are shown in figure 3 and table 1. Photographs of fabricated versions of the antenna are shown in figures 4 and 5.
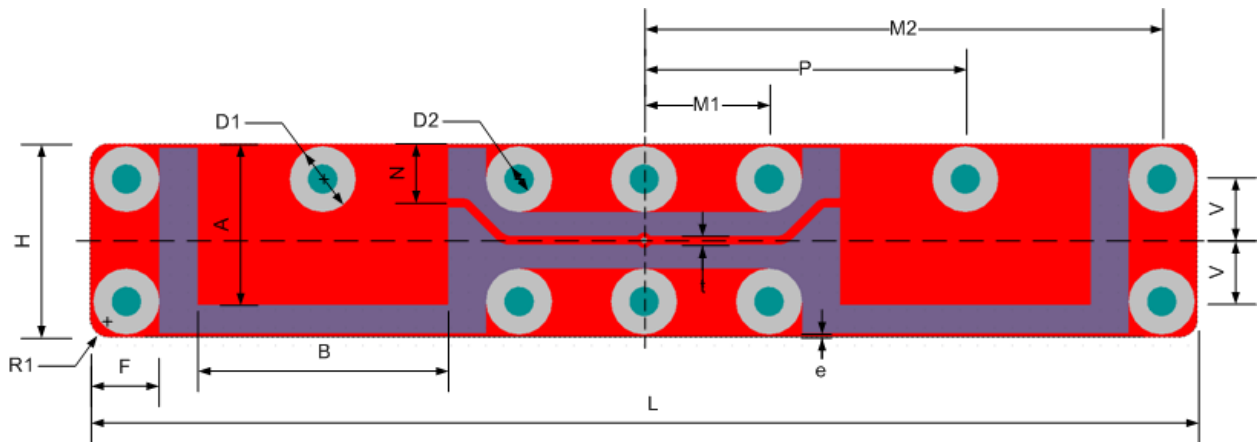
Figure 3
Designed wraparound antenna (flat) with dimensions

Table 1
Antenna dimensions

Name	Description
H	Substrate height
L	Substrate length
A	Element height from top edge
B	Element length (centered on P)
N	Side-feed element matching point
P	Element position
V	Bolt pattern vertical spacing from center
M1	Inner bolt position
M2	Outer bolt position
D1	Plated through hole pad diameter
D2	Plated through hole diameter
R1	Substrate corner radius
F	Edge mounting plating length
e	Edge plating width
t	100-ohm microstrip width

Figure 4
Fabricated wraparound antenna
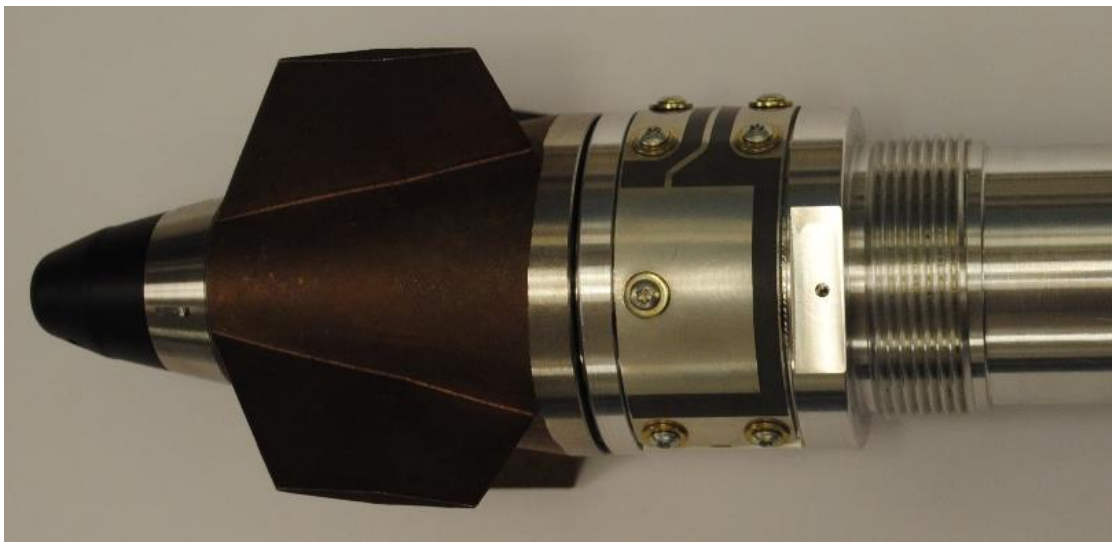
Figure 5
Fabricated wraparound antenna assembled on the ARRT-174 Instrumented PGK

ANTENNA SIMULATIONS

Simulations of the antenna were performed using ANSYS Electromagnetics Suite 2018 (also regarded in industry as Ansoft HFSS) with the geometry shown in figures 6 and 7. An "Interpolating Sweep" between 2 and 2.5 GHz was used for return loss simulations. A single solution at 2.2545 GHz was used for all radiation pattern plots. All geometry is surrounded by a vacuum-filled volume with an outer radiation absorbing layer padded 20 cm away from the projectile geometry.

(a)
Canard position no. 1

(b)
Canard position no. 2
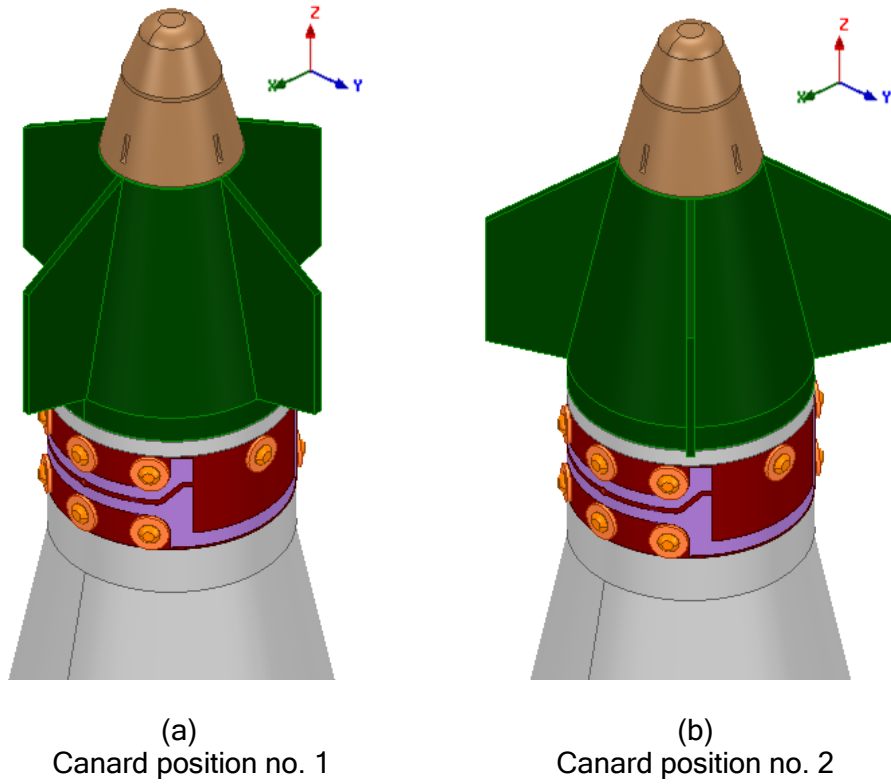
Figure 6
Simulation geometry showing wraparound antenna, PGK, M795 body, and fasteners
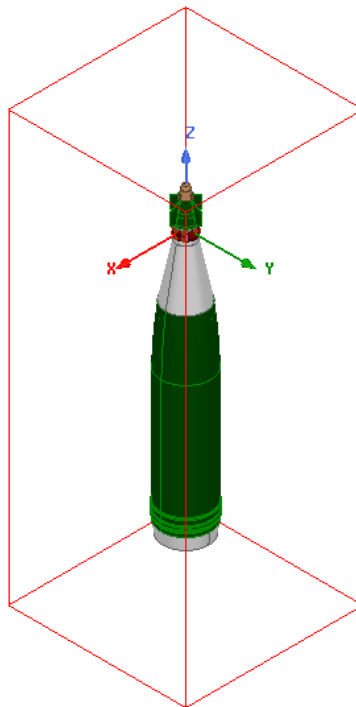
Figure 7
Entirety of simulation geometry, including radiation absorption boundary (red)

The antenna traces were drawn as flat artwork in PTC CREO computer-aided drawing software and then extruded to 1.4-mil height (representative of 1-oz copper on printed circuit boards). The resulting object was then bent virtually around a 2.4-in. diameter cylinder, forming the bent Rogers substrate. These were then imported into ANSYS as "copper" material for the antenna geometry. The 3D models of a PGK and an M483A1 projectile were also imported as the projectile. The projectile body and PGK canards were assigned as "steel" material. The projectile base, ogive, and PGK body were assigned as "aluminum" material. Finally, the PGK nosecone was assigned as "plexiglass" material. Geometry mimicking a 50-ohm coaxial cable with Teflon™ dielectric was included feeding the antenna from within the projectile. Additional models of 4-40 bolts and 0.377-in. diameter washers were also included and assigned as "copper" material. Material properties are given in table 2.

Table 2
Simulation materials and associated properties

| Name	Relative permittivity	Dielectric loss tangent	Relative permeability	Bulk conductivity (s/m)
Steel	1	0	83	4.55e6
Aluminum	1	0	1.000021	3.8e7
Copper	1	0	0.999991	5.8e7
Rogers RT/duroid 5870	2.33	0.0012	1	0
Teflon™	2.1	0.001	1	0
Plexiglass	3.4	0.001	1	0
Vacuum	1	1	0	0

ANTENNA ANALYTICAL MODEL

An analytical model for the antenna radiation pattern can be created by treating it as a pair of diametrically opposed, circumferential narrow slot apertures with uniform-field distributions on an infinite cylinder. These slots are the lower radiating edges of the quarter-wavelength microstrip elements, and it can be assumed that the field distributions within the slots are uniform by assuming that the microstrip elements are operating in TM^{01} mode. The closed-form solutions for the pattern from a single aperture on an infinite cylinder can be found in reference 22, which will be adapted to two apertures using convolution in Fourier space, later in this section. The lengths of the slots used in the model are 68 deg on an infinite 2.4-in. diameter cylinder as shown in figure 8.
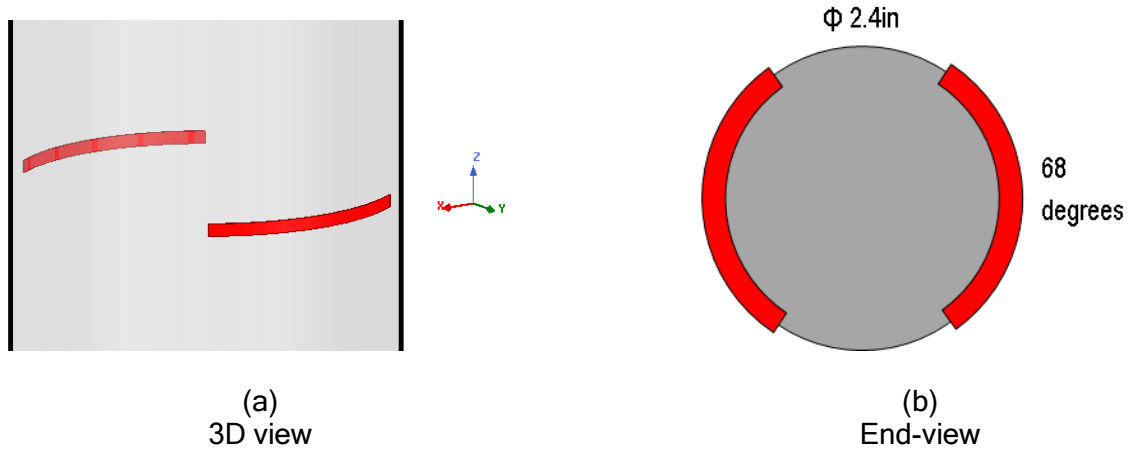
(a)
3D view

(b)
End-view

Φ 2.4in

68 degrees

Figure 8
Circumferential slots on an infinite cylinder

In the far zone, the fields from an arbitrary slot on an infinitely long cylinder of radius $\rho = a$ are represented by a Fourier series (eq. 5-151 in ref. 22):

$$E_\theta \xrightarrow{r=\infty} j\omega\mu \frac{e^{-jkr}}{\pi r} \sin(\theta) \sum_{n=-\infty}^{\infty} e^{jn\phi} j^{n+1} f_n(-k\cos\theta)$$

$$E_\phi \xrightarrow{r=\infty} -jk \frac{e^{-jkr}}{\pi r} \sin(\theta) \sum_{n=-\infty}^{\infty} e^{jn\phi} j^{n+1} g_n(-k\cos\theta)$$

(1)

With functions $f_n(w)$ and $g_n(w)$ defined as (eq. 5-145 in ref. 22):

$$f_n(w) = \frac{j\omega\epsilon \overline{E}_z(n,w)}{(k^2 - w^2) H_n^{(2)}(a\sqrt{k^2 - w^2})}$$

$$g_n(w) = \frac{1}{\sqrt{k^2 - w^2} H_n^{(2)\prime}(a\sqrt{k^2 - w^2})} \left[\overline{E}_\phi(n,w) + \frac{nw}{a(k^2 - w^2)} \overline{E}_z(n,w) \right]$$

(2)

Where functions $H_n^{(2)}$ and $H_n^{(2)\prime}$ are Hankel functions of the second kind of order n and its derivative, respectively. The functions $\overline{E}_\phi(n,w)$ and $\overline{E}_z(n,w)$ are the cylindrical transforms of the tangential components of E on the cylinder. Both functions are a Fourier series on ϕ and a Fourier transform on z. They are defined as follows (eq. 5-144 in ref. 22):

$$\overline{E}_\phi(n,w) = \frac{1}{2\pi} \int_0^{2\pi} d\phi \int_{-\infty}^{\infty} E_\phi(a,\phi,z) e^{-jn\phi} e^{-jwz} dz$$

$$\overline{E}_z(n,w) = \frac{1}{2\pi} \int_0^{2\pi} d\phi \int_{-\infty}^{\infty} E_z(a,\phi,z) e^{-jn\phi} e^{-jwz} dz$$

(3)

For a single circumferential slot of angular length α and vertical width W and assuming a uniform distribution field distribution within that slot:

$$E_z(a,\phi,z) = V$$
$$E_\phi(a,\phi,z) = 0$$

(4)

As the slot becomes narrow ($W \to 0$), the Fourier transform on z becomes unity for all z, leaving only the Fourier series on ϕ:

$$\overline{E}_z(n,w) = \frac{1}{2\pi}\int_{-\alpha/2}^{\alpha/2} d\phi \int_{-\infty}^{\infty} V\,\delta(z)e^{-jn\phi}e^{-jwz}dz = \frac{V}{-jn2\pi}\left(e^{-jn\alpha/2} - e^{jn\alpha/2}\right) =$$

$$\frac{V}{-n\pi}\sin\left(-\frac{n\alpha}{2}\right) = \frac{V\alpha}{2\pi}\operatorname{sinc}\left(\frac{n\alpha}{2}\right) \tag{5}$$

$$\overline{E}_z(n,w) = \frac{V\alpha}{2\pi}\operatorname{sinc}\left(\frac{n\alpha}{2}\right)$$

Where $\operatorname{sinc}(x) = \frac{\sin(x)}{x}$. For two diametrically opposed slots with centers located at 90 and 270 deg, each of equal angular length α:

$$\overline{E}_z(n,w) = \frac{V}{2\pi}\left(\int_{\frac{\pi}{2}-\frac{\alpha}{2}}^{\frac{\pi}{2}+\frac{\alpha}{2}} e^{-jn\phi}d\phi + \int_{\frac{3\pi}{2}-\frac{\alpha}{2}}^{\frac{3\pi}{2}+\frac{\alpha}{2}} e^{-jn\phi}d\phi\right) \tag{6}$$

Which after some manipulation yields:

$$\overline{E}_z(n,w) = \frac{V\alpha}{2\pi}[(-1)^n + 1]j^n \operatorname{sinc}\left(\frac{n\alpha}{2}\right) \tag{7}$$

Far field quantities for a thin single slot therefore become

$$rE_\theta = j\omega\mu\frac{e^{-jkr}}{\pi}\sin(\theta)\sum_{n=-\infty}^{\infty} e^{jn\phi}j^{n+1}\frac{j\omega\epsilon}{k^2\sin^2\theta\, H_n^{(2)}(ka\sin\theta)}\frac{V\alpha}{2\pi}\operatorname{sinc}\left(\frac{n\alpha}{2}\right)$$

$$rE_\theta = \frac{V\alpha}{2j\pi^2}e^{-jkr}\sum_{n=-\infty}^{\infty}\frac{j^n\operatorname{sinc}\left(\frac{n\alpha}{2}\right)}{\sin\theta\, H_n^{(2)}(ka\sin\theta)}e^{jn\phi} \tag{8}$$

$$rE_\phi = -\frac{V\alpha e^{-jkr}\cot\theta}{2\pi^2 ka\sin\theta}\sum_{n=-\infty}^{\infty}\frac{nj^n\operatorname{sinc}\left(\frac{n\alpha}{2}\right)}{H_n^{(2)\prime}(ka\sin\theta)}e^{jn\phi}$$

Far field quantities for two diametrically opposite thin slots become the following equations. $\overline{E}_z(n,w)$ is nonzero only for even values of n.

$$rE_\theta = \frac{V\alpha e^{-jkr}}{j\pi^2\sin\theta}\sum_{\substack{n=-\infty \\ n\,even}}^{\infty}\frac{\operatorname{sinc}\left(\frac{n\alpha}{2}\right)}{H_n^{(2)}(ka\sin\theta)}e^{jn\phi}$$

$$rE_\phi = -\frac{V\alpha e^{-jkr}\cot\theta}{\pi^2 ka\sin\theta}\sum_{\substack{n=-\infty \\ n\,even}}^{\infty}\frac{n\operatorname{sinc}\left(\frac{n\alpha}{2}\right)}{H_n^{(2)\prime}(ka\sin\theta)}e^{jn\phi} \tag{9}$$

It should be noted that the Fourier series of the fields for two diametrically opposite thin slots is the same as the Fourier series of the fields from a single thin slot when multiplied by the Fourier series of a pair of impulse functions representing the slot locations at π and $3\pi/2$. This is the same as convolving the single slot solution with the locations of a circular array, as outlined in references 28 and 29.

Normalized values of the magnitude of the rE_θ pattern[1] for two thin slots are plotted in figure 9. The plot was performed in MATLAB, with source code given in appendix A. The plot is normalized to the magnitude at observation angle $= 90\ deg, \phi = 90\ deg$, directly over the first slot. The summation is calculated for n=-20 to n=20 in steps of 2. The wavenumber k is set as $k = \frac{2\pi}{\lambda}$ where $\lambda = 13.3067\ cm$ (the wavelength of a plane wave in vacuum at 2.2545 GHz). The radius of the cylinder a is set to $a = 3.048\ cm$. The circumferential length of the slots α is set to $\alpha = 68\ deg$. Finally, the excitation voltage of the slots V is set to unity $V = 1$.
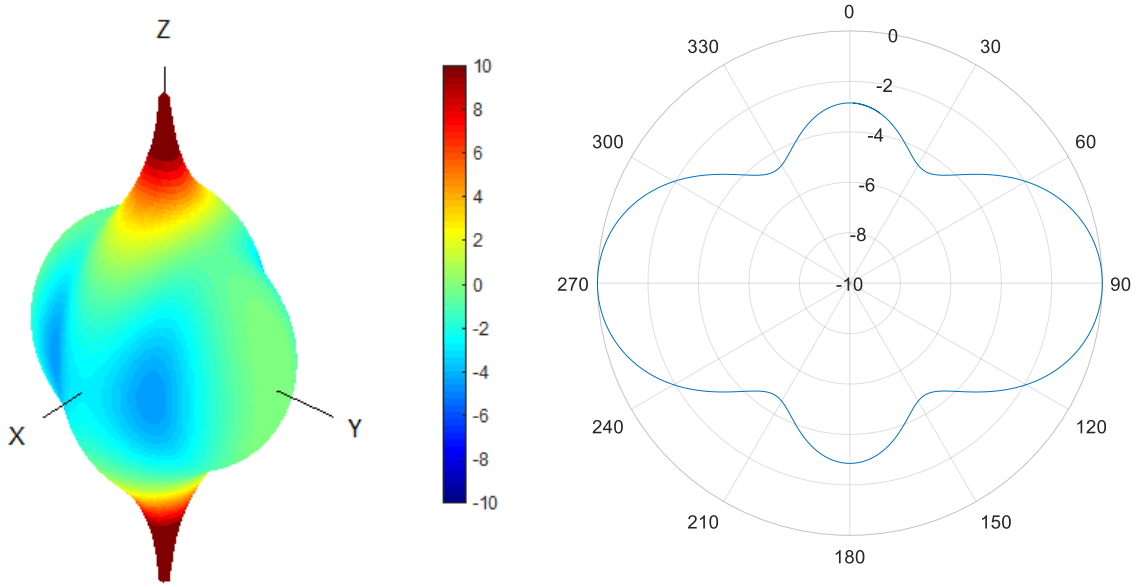

Figure 9
Graphs of normalized Eθ magnitude in dB (first analytical model)

The model predicts 4.66 dB of variation over the roll plane with local minima located at 33, 147, 213, ad 327 deg. Due to the asymptotic approximations for $H_n^{(2)}$ used in this model (eq. 5-142 in ref. 22), which are not valid at $\theta = 0$ and $180\ deg$, this model is limited for predicting quantities only near the $\theta = 90\ deg$ plane.

Another model that can be used that avoids the asymptotic approximations for $H_n^{(2)}$ can be found in equation 5-149 in reference 22, which solves for the near-field and far-field quantities E_z and E_ϕ in cylindrical coordinates outside the cylinder.

$$E_z(\rho, \phi, z) = \frac{1}{2\pi j \omega \epsilon} \sum_{n=-\infty}^{n=\infty} e^{jn\phi} \int_{-\infty}^{\infty} (k^2 - w^2) f_n(w) H_n^{(2)}(\rho\sqrt{k^2 - w^2})\, e^{jwz} dw$$

$$\overline{E}_\phi(\rho, \phi, z) = \frac{1}{2\pi} \sum_{n=-\infty}^{n=\infty} e^{jn\phi} \int_{-\infty}^{\infty} \left[\frac{-nw}{j\omega\epsilon} f_n(w) H_n^{(2)}\left(\rho\sqrt{k^2 - w^2}\right) \right.$$
$$\left. + g_n(w)\sqrt{k^2 - w^2}\, H_n^{(2)\prime}(\rho\sqrt{k^2 - w^2}) \right] e^{jwz} dw \tag{10}$$

---

[1] In equation 5-155 (ref. 22), there is an additional constant k in the equation for E_θ, which did not appear in the previous equations. Normalized graphs of the calculated E_θ magnitudes will not be affected by this additional constant should there have been an error in the derivations or a typographical error in the reference.

Using the previous expression of $f_n(w)$ for two thin slots, solving for $E_z(\rho, \phi, z)$ yields:

$$E_z(\rho, \phi, z) = \frac{V\alpha}{2\pi^2} \sum_{\substack{n=-\infty \\ n\ even}}^{n=\infty} e^{jn\phi} \, j^n \text{sinc}\left(\frac{n\alpha}{2}\right) \int_{-\infty}^{\infty} \frac{H_n^{(2)}(\rho\sqrt{k^2-w^2})}{H_n^{(2)}(a\sqrt{k^2-w^2})} \, e^{jwz} dw \qquad (11)$$

The pattern of E_θ for two thin slots can be approximated from the previous equation by solving for $E_\theta = \sin(\theta)\, E_z(\rho, \phi, z)$ at $\rho = r\,\sin(\theta)$, $z = r\,\cos(\theta)$, where r is a large distance from the slots assumed to be in the far-field of the antenna. The wavenumber k is also assumed to be complex [i.e., some dissipation assumed (ref. 22)] so that $\sqrt{k^2 - w^2}$ is never zero.

The pattern of E_θ at the range $r = 100\ cm$ is evaluated and plotted in figure 10. The MATLAB source code for this model can be found in appendix B. The integral is numerically integrated for values of $w = -200$ to $w = 200$, and the summation is calculated for $n = -20$ to $n = 20$ in steps of 2. The wavenumber k is assumed to be $k = \frac{2\pi}{\lambda} - 0.001i$ where $\lambda = 13.3067\ cm$ (the wavelength of a plane wave in vacuum at 2.2545 GHz). The radius of the cylinder a is set to $a = 3.048\ cm$. The circumferential length of the slots α is set to $\alpha = 68\ deg$. Finally, the excitation voltage of the slots V is set to unity $V = 1$.
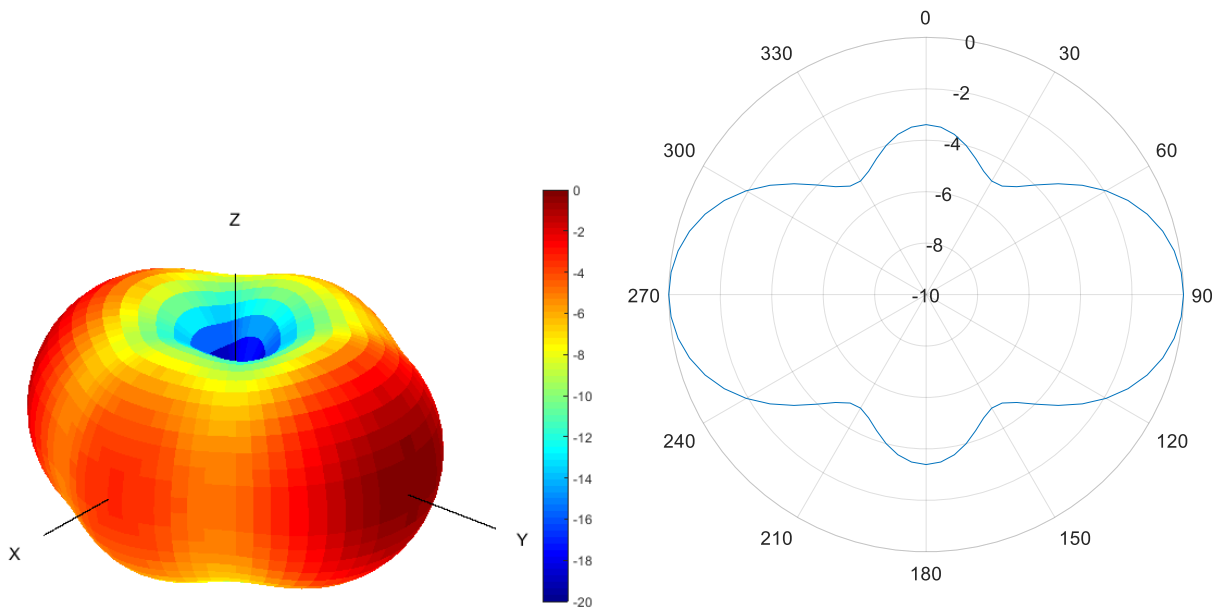

Figure 10
Graphs of normalized E$_\theta$ magnitude in dB (second analytical model)

The model predicts 4.90 dB of variation over the roll plane with local minima located at 60, 120, 240, and 300 deg. The model is also well-behaved as θ approaches 0 and 180 deg. Normalized magnitude plots of E_θ in dB, along the $\phi = 0, 90\ deg$ planes are shown in figure 11.
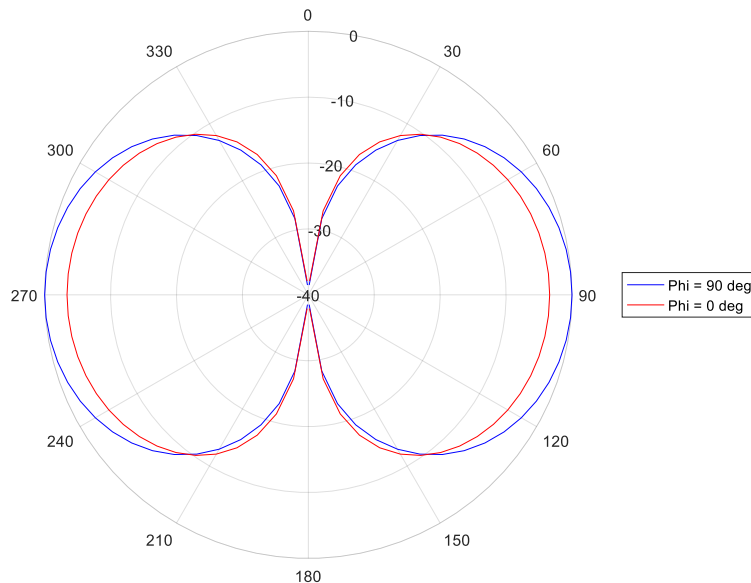
Figure 11
Graphs of normalized E_θ magnitude in dB along elevation planes Phi=0 deg and Phi=90 deg (second analytical model)

ANTENNA MEASUREMENTS

The return loss of the antenna was measured using an HP 8753E vector network analyzer (VNA). The wraparound antenna was assembled onto a PGK shaped housing and then mounted onto a hollow M483A1 projectile body. The VNA was calibrated and connected to a short SubMiniature version A (SMA) coaxial cable feed soldered to the backside of the antenna. Cabling was fed down through the hollow projectile and out of a hole drilled in the projectile base.

The radiation pattern of the antenna was measured in an anechoic chamber (17.20 x 3.35 x 3.35 m, SFC-16 anechoic foam) with its position and orientation controlled by a Diamond Engineering Measurement System Model X100 turntable. Two sets of testing were performed. In the first, the PGK housing was mounted on a full M483A1 projectile, as shown in figure 12. The entire assembly was vertically oriented, placed on top of 1.5 in. of foam sheets, and centered on the positioner turntable. In the second, the PGK housing was mounted to a full M483A1 projectile, which was rested on its side on the positioner turntable, as shown in figure 13. The assembly was supported by 10 in. of foam sheets between it and the turntable surface. A list of equipment used is given in table 3. The antenna gain was derived from the measured received power using the values and formulas shown in table 4.

Note: Vertically positioned to measure pattern in the roll plane.

Figure 12
Anechoic chamber and M483A1 used for radiation pattern testing
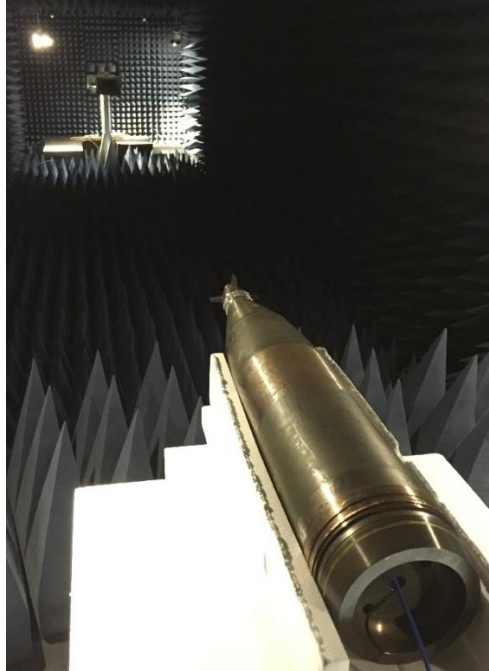
Note: Horizontally positioned to measure
patterns in elevation.

Figure 13
Anechoic chamber and M483A1 projectile used for radiation pattern testing

Table 3
Anechoic chamber test equipment used

Nomenclature	Model	Manufacturer
Receive horn antenna	5GH-1.70	Scientific Atlanta
Wideband amplifier	ZFL-2000+	Mini-Circuits
Power sensor	E4413A	Agilent
Power meter	N1914A	Agilent
Positioner table	X100	Diamond Engineering
Signal generator	7100	Gigatronics

Table 4
Gain calculation values and formulas

Name	Value	Description
f	2.254 GHz	Center frequency
Pt	10.98 dBm	Transmit power (measured at antenna input)
Lp	60 dB	Free space path loss
R	10.5 m	Distance between horn and antenna-under-test
Gr	16.3 dBi	Gain of horn antenna
Ga	19.75 dB	Gain of receive amplifier (with cable losses included)
Lm	1 dB	Mismatch loss
Pr		Power received
Gt	Pr-(Pt-Lm)-Gr-Ga+Lp	Gain of antenna-under-test

The effect of the canard position on the antenna's return loss and radiation pattern was also explored. Measurements were performed with the canard rotated in one of two positions. Canard position no. 1 refers to when the fins are in line with the center of the antenna and its elements. Canard position no. 2 refers to when the fins are rotated 45 deg relative to the center of the antenna and its elements.

Vertically oriented, the antenna and M483A1 shell were placed in the center of the turntable and rotated to gather the radiation pattern in the roll plane, as shown in figure 12. This pattern was measured twice with receiver horn antenna polarized vertically [referred to as co-polarization (co-pol)] and horizontally [referred to as cross-polarization (cross-pol)].

Horizontally oriented, the antenna and M483A1 projectile were placed on the turntable and rotated sideways to gather the radiation pattern in two elevation planes, as shown in figure 13. The first elevation plane (Phi = 0) refers to the YZ plane intersecting the antenna patch elements and was performed with the feed of the antenna pointed skyward. The second elevation plane (Phi = 90) refers to the XZ plane intersecting the antenna feed and was performed with the feed pointing sideways. Each plane was measured twice with receive horn antenna polarized vertically (referred to as cross-polarization) and horizontally (referred to as co-polarization).

MEASUREMENT AND SIMULATION RESULTS

Return Loss

The results of the simulated and measured return losses in canard positions nos. 1 and 2 are shown in figure 14. The minimum measured return loss was detected at -10.62 dB at 2.2689 GHz in canard position no.1 and -11.79 dB at 2.2695 GHz in canard position no. 2. The minimum simulated return loss was -12.00 dB at 2.2660 GHz in canard position no. 1 and -12.41 dB at 2.2560 GHz in canard position no. 2.
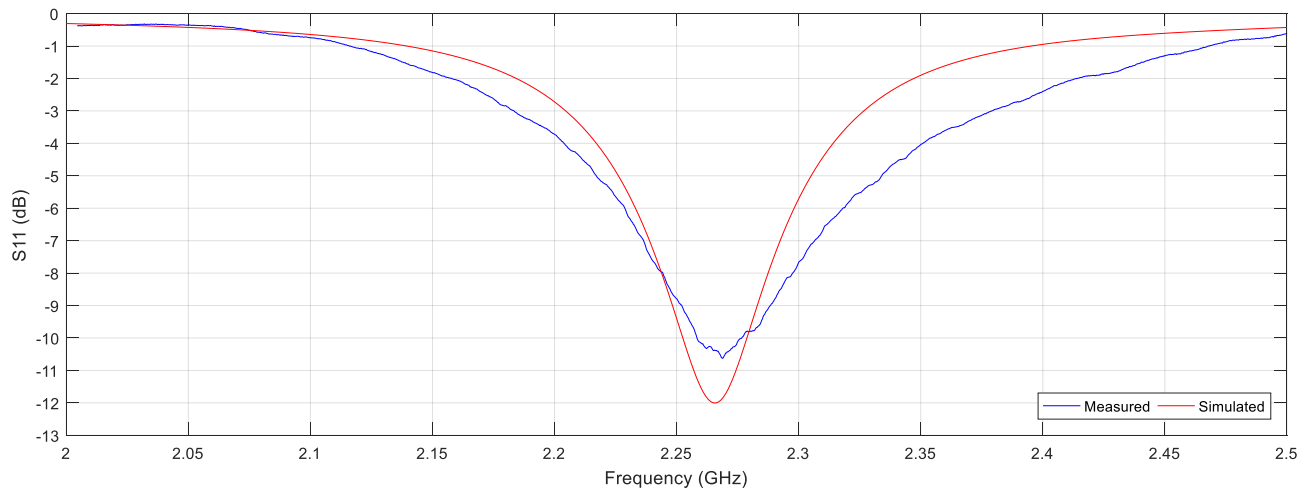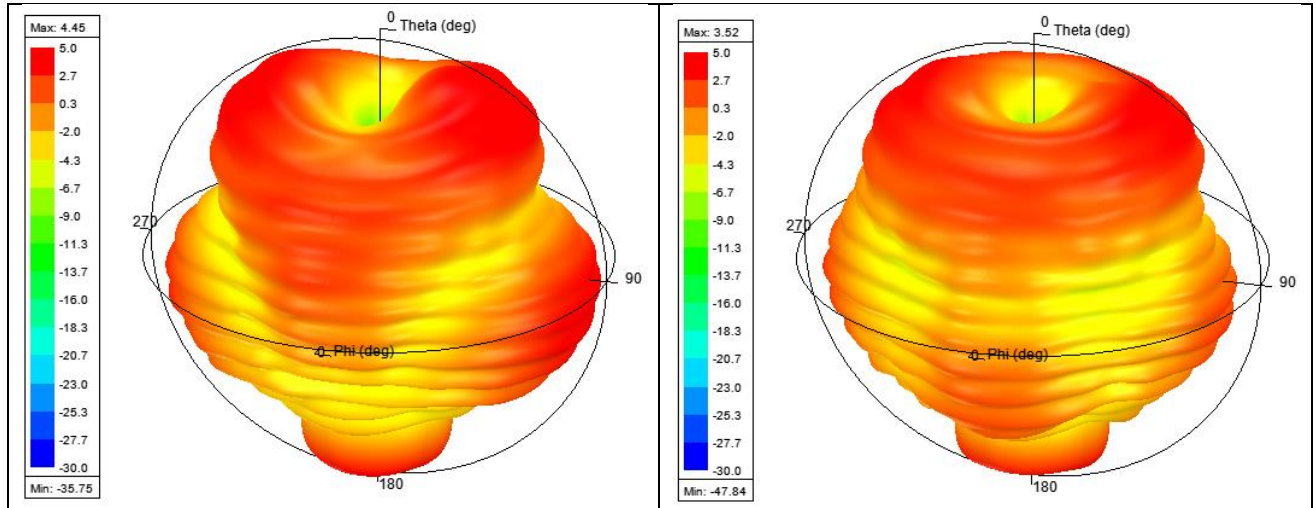
Figure 14
Measured and simulated return loss plots [return loss (dB) versus frequency] – top: canard position no.1, bottom: canard position no. 2

The impedance bandwidth of the antenna (defined as when the return loss is less than -10 dB) in canard position no. 1 was measured to be 17.8 MHz from 2.2585 to 2.2763 GHz. This is in good agreement with the simulated bandwidth of 25 MHz from 2.2530 to 2.2780 GHz. Both are narrower than in canard position no. 2, which was measured to be 37.2 MHz from 2.2485 to 2.2857 GHz. This is in close agreement with the simulated bandwidth of 30 MHz from 2.2410 to 2.2710 GHz.

Radiation Pattern at 2.254 GHz

The antenna's radiation pattern at the intended operating frequency of 2.254 GHz is shown in this section. The 3D plots of the simulated radiation pattern are given in figures 15 and 16. The plots show the theta-polarized gain and the phi-polarized gain patterns of the antenna, in the two canard positions. The plots resemble those of the second analytical model shown previously in figure 10, but with added rippling and irregularities caused by diffraction from the finite-length projectile body, which don't occur on the infinite-length cylinder of that model. Further helping to illustrate the

radiation pattern, the E-field magnitude at a moment in time on the YZ, XZ, and XY planes are shown in figures 17 and 18. If animated, these plots would show the waves radiating outward from the body of the projectile, along with surface wave diffraction occurring down the sides of the projectile.

(a)
Canard position no. 1

(b)
Canard position no. 2

Figure 15
3D rendering of simulated antenna radiation pattern (GainTheta in dBi)

(a)
Canard position no. 1
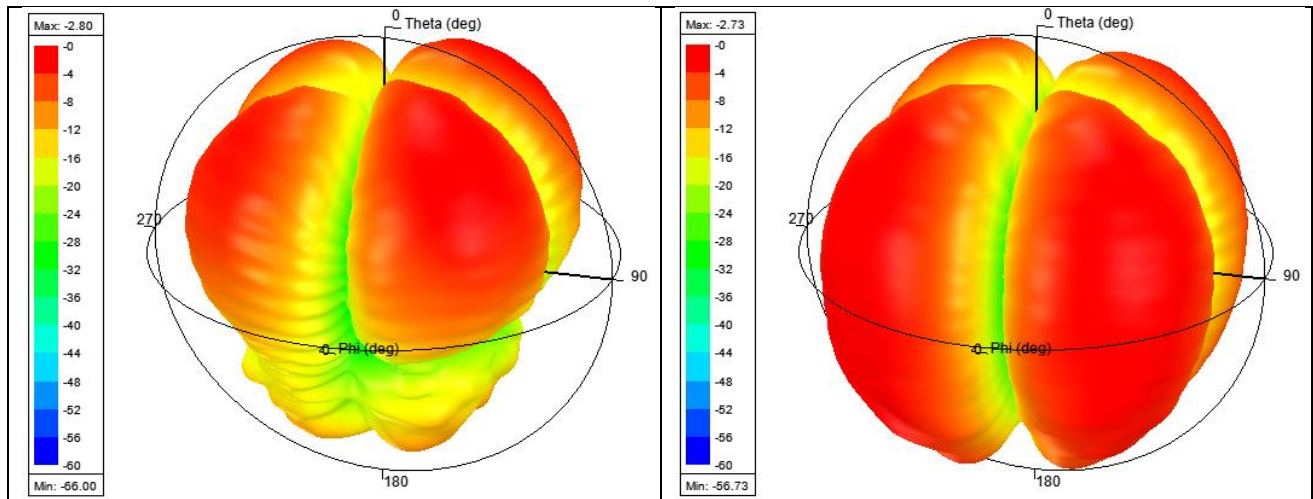
(b)
Canard position no. 2

Figure 16
3D rendering of simulated antenna radiation pattern (GainPhi in dBi)
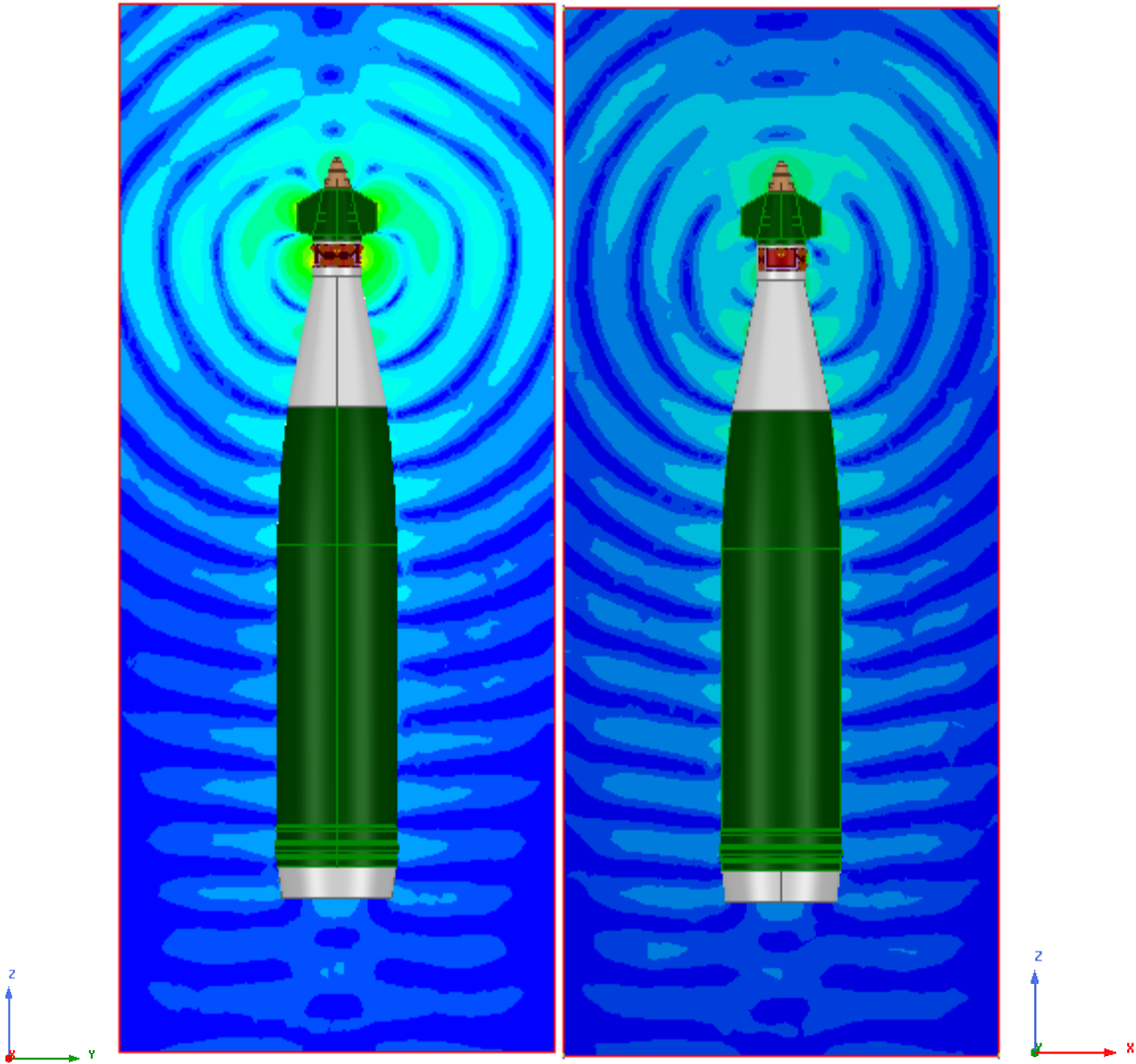
Figure 17
E-field magnitude plot in the YZ and XZ planes

UNCLASSIFIED
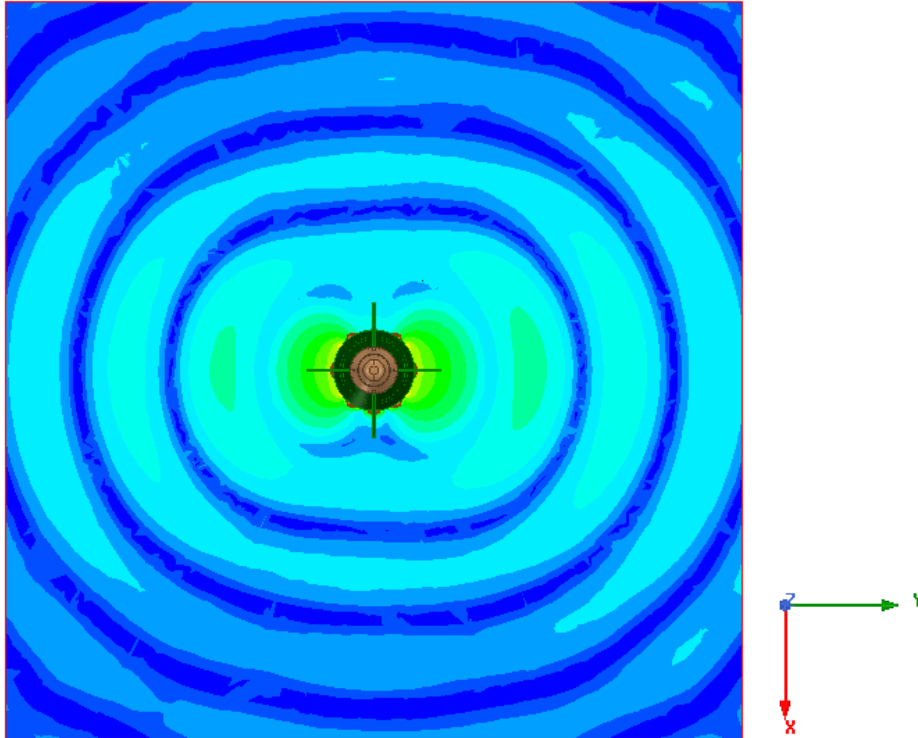
Figure 18
E-field magnitude plot in the XY plane

Polar plots of both the simulated and measured radiation patterns along the Phi=0 and Phi=90-deg elevation planes are shown in figures 19 through 22. Co-pol corresponds to GainTheta in the simulations, while Cross-Pol corresponds to GainPhi. The patterns show local maxima directly over the +Y and -Y axes, which corresponds with directly over the radiating edges of the quarter-wavelength patches. Two deep nulls were located at the +Z and -Z axes, corresponding to the tip and tail of the projectile.

(a)
Canard position no. 1

(b)
Canard position no. 2
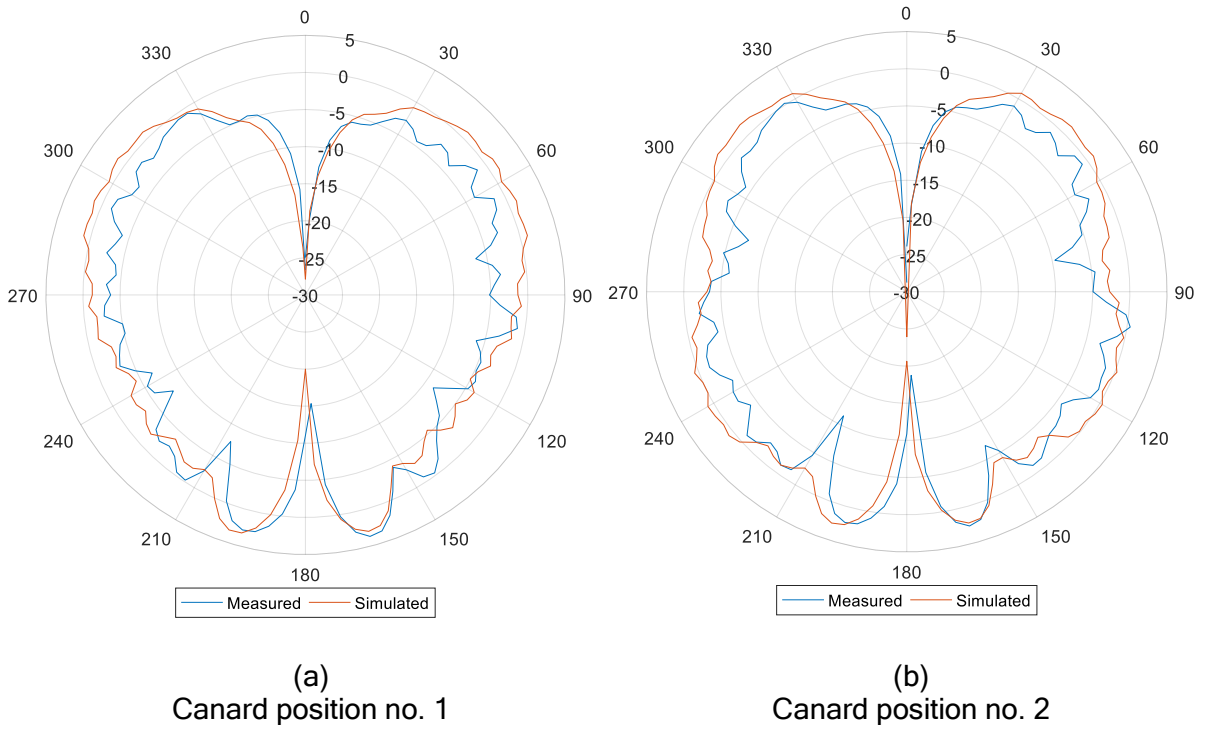
Figure 19
Measured and simulated co-pol radiation pattern at 2.254 GHz – elevation Plane (Phi = 0)

(a)
Canard position no. 1

(b)
Canard position no. 2
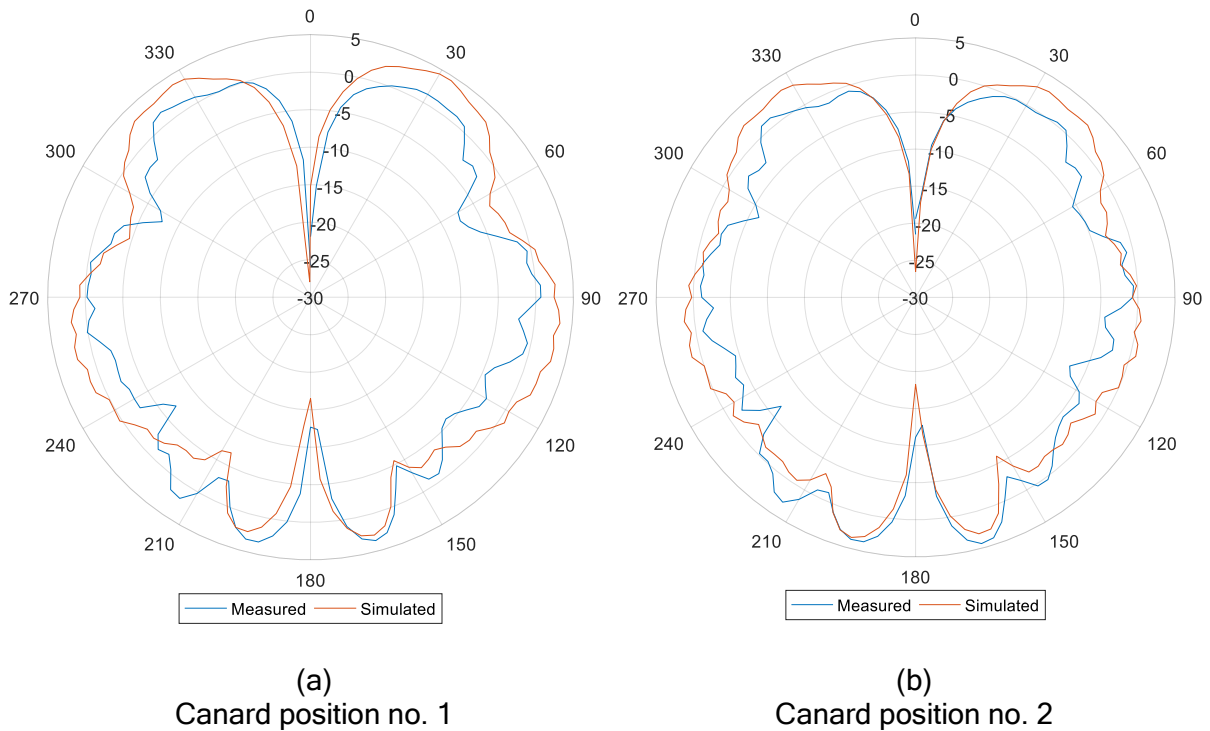
Figure 20
Measured and simulated co-pol radiation pattern at 2.254 GHz – elevation plane (Phi=90)

(a)
Canard position no. 1

(b)
Canard position no. 2
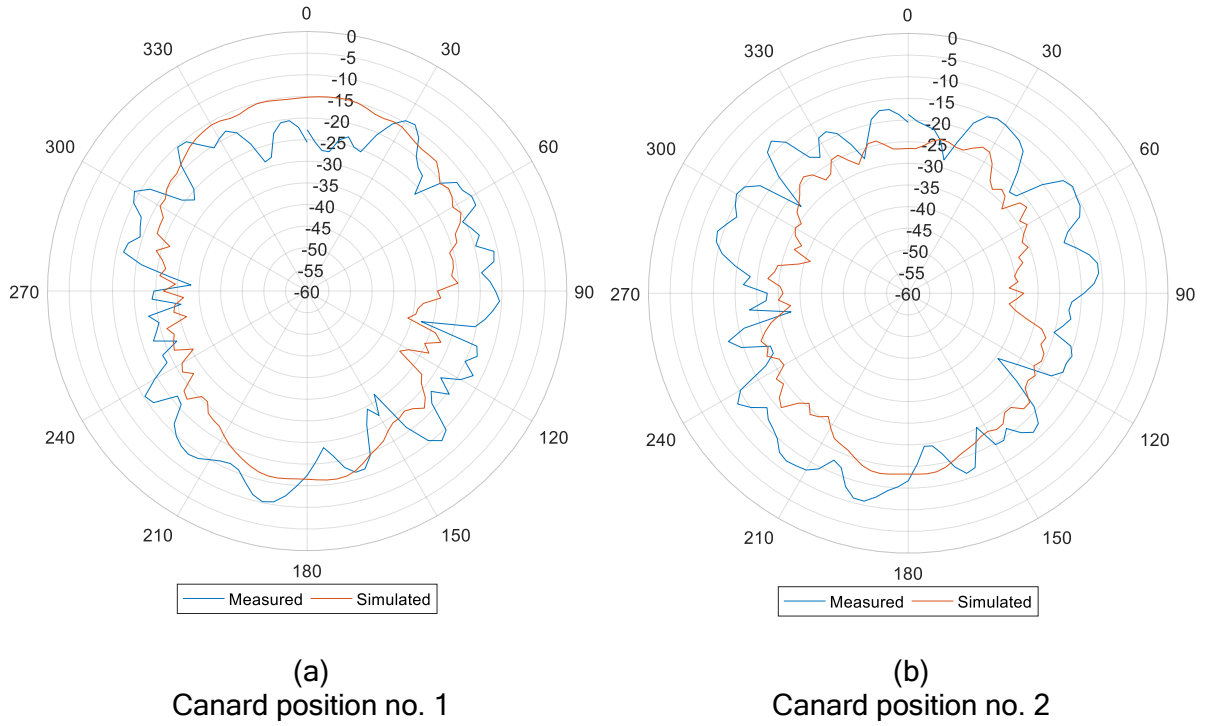
Figure 21
Measured and simulated cross-pol radiation pattern at 2.254 GHz – elevation plane (Phi = 0)

(a)
Canard position no. 1

(b)
Canard position no. 2

Figure 22
Measured and simulated cross-pol radiation pattern at 2.254 GHz – elevation plane (Phi=90)

The antenna's radiation pattern in the two elevation planes (XZ and YZ) at 2.254 GHz is shown in the previous figures. The maximum gain measured was 3.70 dBi in canard position no. 1 and 4.37 dBi in canard position no. 2, both at elevation angles of 165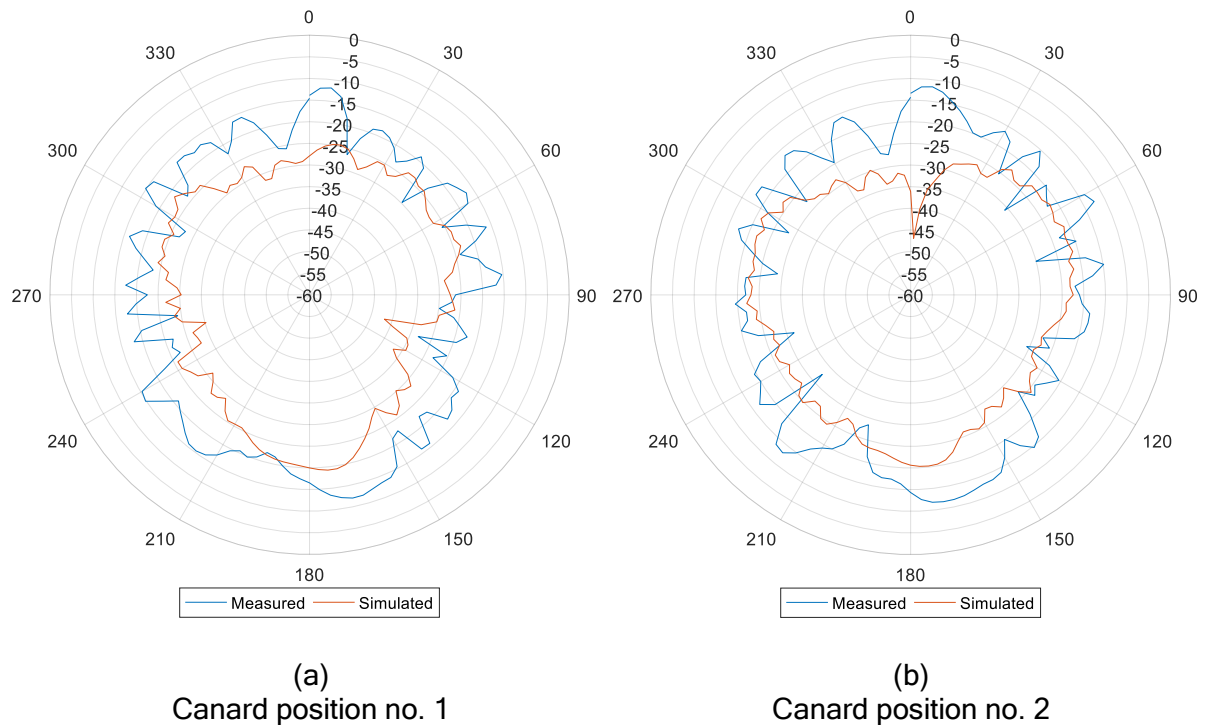 deg from the nose (15 deg from the tail). Angular coverage of the antenna (herein defined as gain > -10 dBi regardless of canard position) was measured as 141 deg, from 9 to 150 deg from the nose. Measured gain is maximized toward the rear of the projectile (15 deg from the tail) and is due to surface diffraction from the projectile body.

Simulation predicted maximum gain of 4.39 dBi in canard position no. 1 at 33 deg from the nose and 3.51 dBi in canard position no. 2 at 195 deg from the nose (15 deg from the tail). Measure and simulated patterns are in good agreement with simulation predicting slightly higher gain. Angular coverage is also in good agreement with simulation, which yielded an angular coverage of 162 deg, from 12 to 174 deg from the nose. Both measurement and simulation show a minor null occurring at nose, tail, and 27 deg from the tail, all of which limits angular coverage. Cross-pol simulation and measurement results are shown in figures 21 and 22.

The antenna's co-polarized radiation pattern in the roll plane at 2.254 GHz is shown in figure 23. Measurement and simulation (GainTheta) are again in good agreement. Maximum gain measured in this plane was 2.03 dBi in canard position no.1 and 1.07 dBi in canard position no. 2, both occurring at Phi= 93 deg. Minimum gain was -6.16 dBi occurring at Phi=210 deg in canard position no. 1 and -6.27 dBi occurring at Phi=213 deg in canard position no. 2. Maximum predicted gain from simulation was 2.42 dBi occurring at Phi=90 deg in canard position no. 1 and 0.20 dBi occurring at Phi=270 deg in canard position no. 2. Minimum prediction gain from simulation was -5.70 dBi occurring at Phi=219 deg in canard position no. 1 and -6.55 dBi occurring at Phi=144 deg in canard position no. 2. Cross-polarization simulation and measurement (GainPhi) results in the roll plane are shown in figure 24.

(a)
Canard position no. 1

(b)
Canard position no. 2
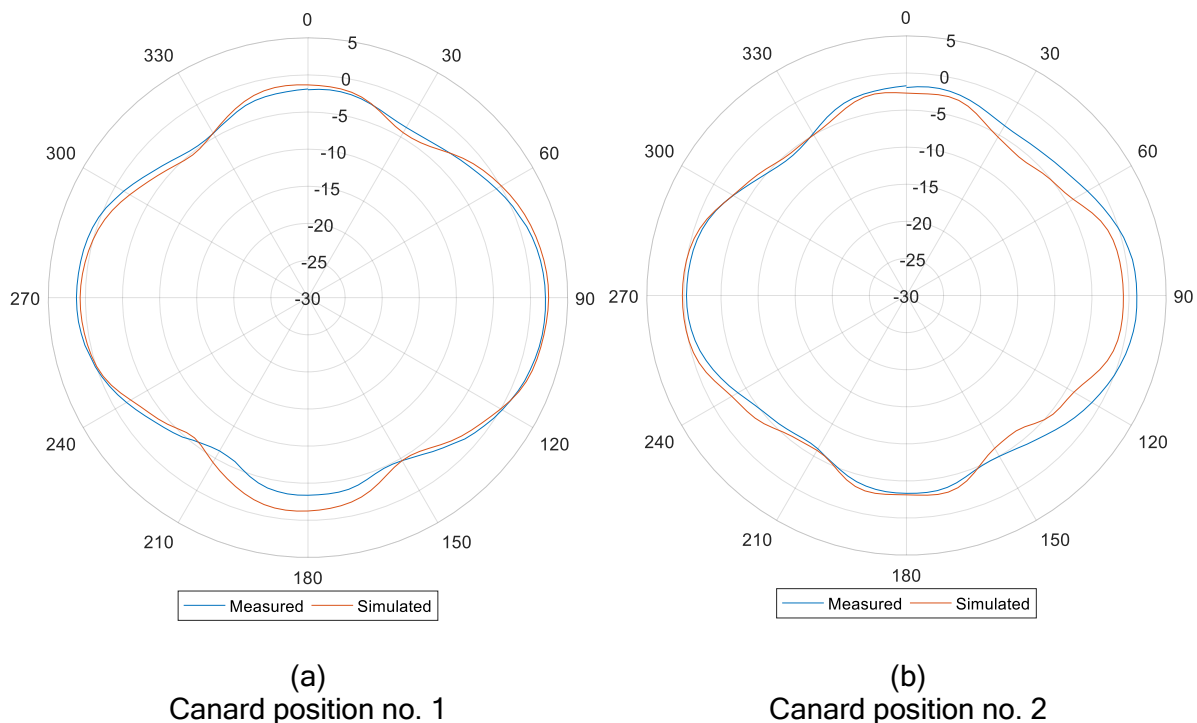
Figure 23
Measured and simulated (co polarization) pattern at 2.254 GHz – roll plane

(a)
Canard position no. 1

(b)
Canard position no. 2
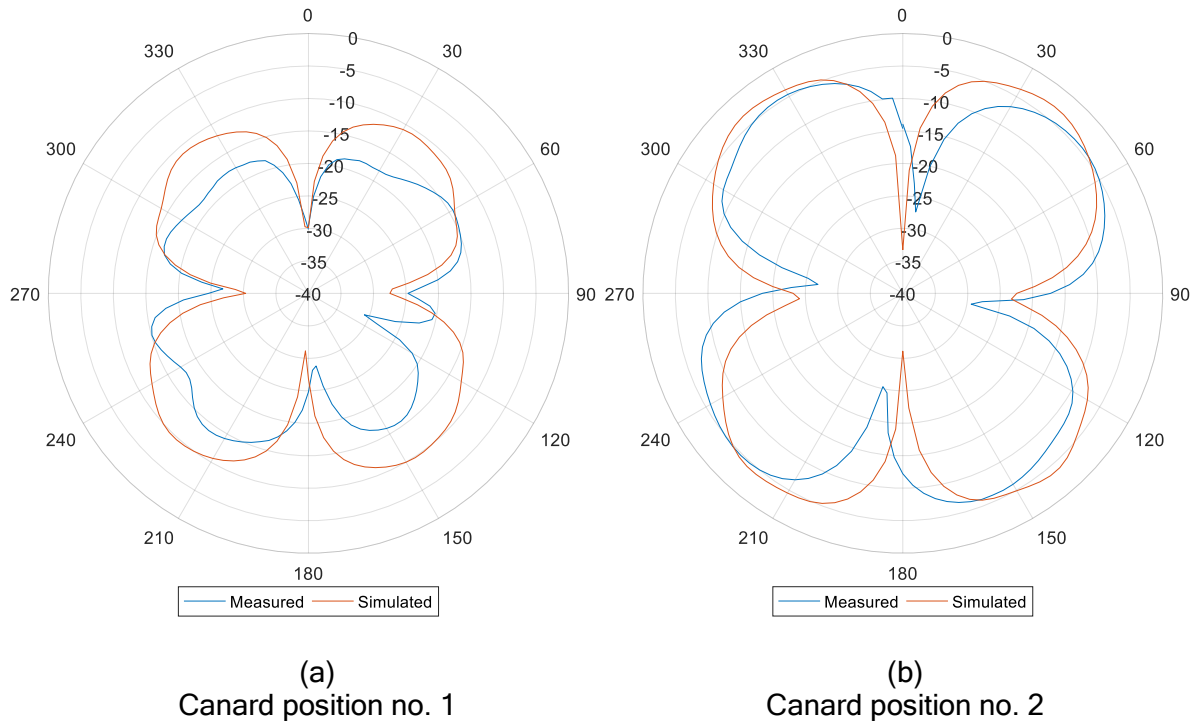
Figure 24
Measured and simulated (cross polarization) pattern at 2.254 GHz – roll plane

CONCLUSIONS

The designed wraparound antenna can be used in smart munitions for S-band telemetry and other radio services. It has been tested on 155-mm artillery platforms with success. The antenna is small, inexpensive to produce, and requires no external matching components. It is designed for typical use on 1 to 3-in. diameter cylindrical housings but can be used on larger diameters as well. The performance of the antenna, wrapped on a Precision Guidance Kit-shaped housing was modeled and validated by measurements in an anechoic chamber and with a network analyzer. Two analytical models that predict the radiation pattern of the antenna were explored using MATLAB. The measurements show that the antenna operates at the intended frequency and provides adequate coverage azimuthally around the body of the munition with minimal roll plane variation.

REFERENCES

1. Barton, A., "Nosecone Inverted-F Antenna (IFA) for S-band Telemetry," Technical Report ARMET-TR-16075, U.S. Army ARDEC, Picatinny Arsenal, NJ, September 2017.

2. Katulka, G., Hall, R., Topper, B., and Hundley, N., "Design and Analysis of Embedded Antennas for 60-mm Mortars," Technical Report ARL-TR-4483, U.S. Army Research Laborator, Aberdeen Proving Ground, MD, June 2008.

3. Grzybowski, D. M., Peregino, P. J., and Davis, B. S., "Development of a Telemetry-Enabled High-G Projectile Carrier," Technical Report ARL-TR-6099, U.S. Army Research Laboratory, Aberdeen Proving Ground, MD, September 2012.

4. Ryken, Jr., M. L. and Davis, A. F., "TM microstrip antenna with GPS frequency coverage," U.S. Patent, US7193567 B1, 2005.

5. Munson, R. E., "Conformal Microstrip Antennas and Microstrip Phased Arrays," IEEE Transactions on Antennas and Propagation, January 1974.

6. Krutsinger, J. and Munson, R., "Single slot cavity antenna assembly," U.S. Patent, US3713162 A, 1973.

7. Reggia, F. and Jones, Jr., H. S., "Very thin (wrap-around) conformal antenna," U.S. Patent, US 4110751 A, 1978.

8. Byron, E. V., "A new flush-mounted antenna element for phased array application," in Proc. Phased-Array Antenna Symp, pp.187-192, 1970.

9. Howell, J. Q., "Microstrip Antennas," IEEE Transactions on Antennas and Propagation, vol. 23, no.1, pp.90-93, January 1975.

10. Bernhard, J. T., Mayes, P. E., Schaubert, D., and Mailloux, R.J., "A Commemoration of Deschamps and Sichak's Microstrip Microwave Antennas: 50 Years of Development Divergence and New Directions", Proceedings of the 2003 Antenna Applications Symposium (27th) Held in Monticello, Illinois on 17-19, Volume 1, DTIC ADA429122, September 2003.

11. Deschamps, G. and Sichak, W., "Microstrip Microwave Antennas," Proceedings of the Third Symposium on the USAF Antenna Research and Development Program, October 18-22, 1953.

12. Hall, P. S. and James, J. R., "A Survey of Flat Profile Microwave Antennas," Royal Military College of Science Shrivenham (England) Dept of Electrical and Electronic Engineering, Technical Note, DTIC ADA116834, April 1977.

13. King, R., "Tranmission-Line Missle Antennas," IRE Transactions on Antennas and Propagation, Jan 1960.

14. Schaubert, D., Jones, H., and Reggia, F., "Conformal dielectric-filled edge-slot antennas with inductive-post tuning," IEEE Transactions on Antennas and Propagation, Volume: 27, Issue: 5, September 1979.

15. Sengupta, D. and Martins-Camelo, L., "Theory of dielectric-filled edge-slot antennas," IEEE Transactions on Antennas and Propagation, Volume: 28, Issue: 4, July 1980.

REFERENCES
(continued)

16. Jones, Jr., H.S., "Conformal and Small Antenna Designs," Technical Report HDL-TR-1952, U.S. Army ERADCOM, U.S. Army Materiel Command, Redstone Arsenal, AL, April 1981.

17. Ryken, Jr., M. L., Davis, A. F., and Kujiraoka, S. R., "GPS and telemetry antenna for use on projectiles," U.S. Patent, US 6466172 B1, 2001.

18. Ryken, Jr., M. L. and Davis, A. F., "Multipurpose microstrip antenna for use on missile," U.S. Patent, US 20030076261 A1, 2002.

19. Ryken, Jr., M. L. and Davis, A. F., "TM microstrip antenna," U.S Patent, US 7109929 B1, 2003.

20. Lee, K.-F. and Tong, K.-F., "Microstrip Patch Antennas–Basic Characteristics and Some Recent Advances," Proceeedings of the IEEE, 29 February 2012.

21. Krowne, C. M., "Cylindrical-Rectangular Microstrip Antenna," IEEE Transactions on Antennas and Propagation, January 1983.

22. Harrington, R. F., "Time-Harmonic Electromagnetic Fields," Chapter 5 (Cylindrical Wave Functions), Section 12 (Apertures in Cylinders), 1961.

23. James, J. R. and Hall, P. S., "Handbook of Microstrip Antennas," Technology & Engineering, Peter Peregrinus Ltd., London, United Kingdom,1989.

24. Ashkenazy, J., Shtrikman, S., and Treves, D., "Electric Surface Current Model for the Analysis of Microstrip Antennas on Cylindrical Bodies," IEEE Transactions on APS, March 1985.

25. Perlmutter, P., Shtrikman, S., and Treves, D., "Electric surface current model for the analysis of microstrip antennas with application to rectangular elements," IEEE Transactions on Antennas and Propagation, Volume: 33, Issue: 3, March 1985.

26. Balanis, C., "Radiation From Slots On Cylindrical Bodies Using Geometrical Theory Of Diffraction and 'Creeping Wave Theory'," NASA TR R-331, 1970.

27. Barton, A., "Antenna Detuning on Projectiles," Technical Report ARMET-TR-18019, U.S. Army CCDC AC, Picatinny Arsenal, NJ, May 2020.

28. Josefsson, L. and Persson, P., "Conformal Array Antenna Theory and Design," John Wiley & Sons, February 2006.

29. Wait, J., and Householder, J., "Pattern Synthesis for Slotted-Cylinder Antennas," Journal of Research of the National Bureau of Standards, Vol. 63D, No. 3, November to December 1959.

APPENDIX A
MATLAB SOURCE CODE FOR FIRST ANALYTICAL MODEL

```matlab
%%Predictor of radiation pattern from two diametrically opposed,
%infinitely thin, circumferential slots, using asymptotic relations
lambda = 30/2.2545;  % Wavelength in centimeters
k = 2*pi/lambda;     % Wavenumber
V = 1;               % Amplitude of E-field magnitude within slot, usually 1


alpha = 68*pi/180;   % Circumferential length of slot in radians.
                     % Note: alpha = Pi/N makes besselh becomes Inf
a = 3.048;           % Radius of cylinder in centimeters

theta = (1:1:180)*pi/180;   % Observation angles of Elevation in radians
phi = (1:1:370)*pi/180;     % Observation angles of Azimuth in radians
sum_size = 20;              % Summation Range, will be -sum_size:2:sum_size

e_theta = zeros(length(theta),length(phi)); % Magnitude of theta component of the
E-field. Pre-allocating for speed

% p and t are indexes for phi and theta arrays
for p = 1:1:length(phi)
    for t = 1:1:length(theta)
        % Solve for sigma summation using a loop
        sigma = 0;
        for n = -sum_size:2:sum_size  %even only
            sigma = sigma + (sinc(n*alpha/2/pi)*exp(1i*n*phi(p)))/ ...
                (besselh(n,2,k*a*sin(theta(t))));
        % Note, sinc in matlab is sin(pi*x)/(pi*x). Hence the need for /pi
        end;
        e_theta(t,p) = V*alpha/(1i*pi^2*sin(theta(t)))*sigma;
    end
end;

%% Convert to dB and normalize to E_theta at Phi= 90 deg, and Theta= 90 deg,
% directly over the first slot.
e_theta_db = 10*log10(abs(e_theta.*conj(e_theta)));
e_theta_db_norm = e_theta_db-max((e_theta_db(90,90)));

%% Plot 3D Pattern

%Set range of plot in dB
mindb =-20;
maxdb = 20;

%Setup Meshplot
n = 1; %Used for skipping phi,theta angles
[az,el] = meshgrid(phi(1:n:end)/pi*180,theta(1:n:end)/pi*180);
d = e_theta_db_norm(1:n:end,1:n:end);
d2 = (d-mindb)./(maxdb-mindb); % Normalize values between 0-1 dB
%Clip to values between 0-1 dB
d2(d2 < 0) = 0;
d2(d2 > 1) = 1;

%Generate plot
figure();
[x,y,z] = sph2cart((az)*pi/180,(el-90)*pi/180,d2);
surf(x,y,z,d,'LineStyle','none');
caxis([mindb+10 maxdb-10]);
```

```matlab
colorbar;
colormap jet;
axis equal
shading faceted
axis off;
set(gcf,'color','w');

%Draw axes in plot
xl = xlim();
yl = ylim();
zl = zlim();
hold on;
line([0 1.5*xl(2)], [0,0], [0,0], 'LineWidth', 1, 'Color', 'k');
line([0,0], [ 0 1.5*yl(2)], [0,0], 'LineWidth', 1, 'Color', 'k');
line([0,0], [0,0], [ 0 1.1*zl(2)], 'LineWidth', 1, 'Color', 'k');
text(0,0,zl(2)+0.25,'Z','fontsize',12,'horizontalalignment','center');
text(0,yl(2)+0.35,0,'Y','fontsize',12,'horizontalalignment','center');
text(xl(2)+0.35,0,0,'X','fontsize',12,'horizontalalignment','center');
hold off;

%% Plot Roll Plane
figure();
polarplot(phi,e_theta_db_norm(90,:));rlim([-10 0]);
pax = gca;
pax.ThetaZeroLocation = 'top';
pax.ThetaDir = 'clockwise';
set(gcf,'color','w');
```

APPENDIX B
MATLAB SOURCE CODE FOR SECOND ANALYTICAL MODEL

```matlab
%% Predictor of radiation pattern from two diametrically opposed,
% circumferential slots with width, without asymptotic relations,
%using Ez calculated at an explicit range

lambda = 30/2.2545;   % Wavelength in centimeters
k = 2*pi/lambda-0.001*1i; % Wavenumber with small loss
V = 1;                 % Amplitude of E-field magnitude within slot, usually 1
W = 0.15748;           % Slot width in centimeters


alpha = 68*pi/180;     % Circumferential length of slot in radians.
                       % Note: alpha = Pi/N makes besselh becomes Inf
a = 3.048;             % Radius of cylinder in centimeters

theta = [0.1 [5:5:175] 179.9] *pi/180; %Observation angles of Elevation in
radians. NaN is encountered at 0 and 180 degrees, so 0.1 and 179.9 are used
instead
phi = (0:5:360)*pi/180;      % Observation angles of Azimuth in radians

range = 100; % Observation range from origin for E_z

%Calculate cylindrical coordinates (rho,z) from spherical coordinates (theta,phi)
at range
rho = range*sin(theta); % Observation rho
z = range*cos(theta); %0:0.1:10; % Observation z

sum_size = 40; % Summation Range, will be -sum_size:2:sum_size
w_size = 200; %Range of integral over w, will be -w_size:2:w_size;

%Magnitude of z component of the E-field. Preallocating for speed
e_z = zeros(length(theta),length(phi));

%To make this fast, rather than solve the equation at every theta,phi pair
%like the previous model:
%1)  Create an array "term_phi" of all the terms of e^(j*n*phi), for all n in
n_range (rows), and all phi (columns)
%2)  At each theta, solve for the portions of the terms of the finite sum
%       only dependent on theta, and gather these into a column vector
"term_theta"
%3)  Multiply term_theta with the columns of term_phi, and sum through the
%    columns. Then multiple by V*alpha/(2*pi^2). This vector is e_z for
%    all phi, at that theta.
%
n_range = (-sum_size:2:sum_size)';% Create array of indexes of the finite sum
term_phi = exp(1i*n_range*phi); % Create term_phi array, (1) from above
```

```matlab
for t = 1:1:length(theta)
    for n = 1:1:length(n_range)
        % (2) from above
        fun = @(w)(besselh(n_range(n),2,rho(t).*sqrt(k.^2-(w).^2))./ ...
            besselh(n_range(n),2,a*sqrt(k.^2-(w).^2)).*exp(1i*w*z(t)));

        term_theta(n,1) = (((-1)^n_range(n)+1)*(1i)^n_range(n)).* ...
        sinc(n_range(n)*alpha/2/pi)* ...
        integral(fun,-w_size,w_size,'RelTol',1e-10,'AbsTol',1e-12);
    end;
    % (3) from above
    e_z(t,:) = V*alpha/(2*pi^2)*sum(repmat(term_theta,1,length(phi)).*term_phi);

end;

%% Convert to E_theta, then to dB and normalize to max E_theta
e_z_outside = e_z.*repmat((rho > a)',1,length(phi)); %Remove all values within
the cylinder
e_th = e_z_outside.*repmat(sin(theta)',1,length(phi)); %Convert E_z to E_theta
e_th_db = 10*log10(abs(e_th.*conj(e_th)));   %Convert to dB
e_th_db_norm = e_th_db-max(max((e_th_db)));

%% Plot 3D Pattern

%Set range of plot in dB
mindb =-30;
maxdb = 0;

%Setup Meshplot
n = 1; %Used for skipping phi,theta angles
[az,el] = meshgrid(phi(1:n:end)/pi*180,theta(1:n:end)/pi*180);
d = e_th_db_norm(1:n:end,1:n:end);
d2 = (d-mindb)./(maxdb-mindb); % Normalize values between 0-1 dB
%Clip to values between 0-1 dB
d2(d2 < 0) = 0;
d2(d2 > 1) = 1;

%Generate plot
figure();
[x,y,z] = sph2cart((az)*pi/180,(el-90)*pi/180,d2);
surf(x,y,z,d,'LineStyle','none');
caxis([mindb+10 maxdb]);
colorbar;
colormap jet;
axis equal
shading faceted
axis off;
set(gcf,'color','w');

%Draw axes in plot
xl = xlim();
yl = ylim();
zl = zlim();
hold on;
line([0 1.5*xl(2)], [0,0], [0,0], 'LineWidth', 1, 'Color', 'k');
line([0,0], [ 0 1.5*yl(2)], [0,0], 'LineWidth', 1, 'Color', 'k');
line([0,0], [0,0], [ 0 1.1*zl(2)], 'LineWidth', 1, 'Color', 'k');
```

```matlab
text(0,0,zl(2)+0.25,'Z','fontsize',12,'horizontalalignment','center');
text(0,yl(2)+0.35,0,'Y','fontsize',12,'horizontalalignment','center');
text(xl(2)+0.35,0,0,'X','fontsize',12,'horizontalalignment','center');
hold off;

%% Plot Roll Plane
figure();
polarplot(phi,e_th_db_norm(find(phi == pi/2),:));rlim([-10 0]);
pax = gca;
pax.ThetaZeroLocation = 'top';
pax.ThetaDir = 'clockwise';
set(gcf,'color','w');
```

DISTRIBUTION LIST

U.S. Army CCDC AC
ATTN: FCDD-ACE-K
Picatinny Arsenal, NJ 07806-5000

Defense Technical Information Center (DTIC)
ATTN: Accessions Division
8725 John J. Kingman Road, Ste 0944
Fort Belvoir, VA 22060-6218

GIDEP Operations Center
P.O. Box 8000
Corona, CA 91718-8000
gidep@gidep.org

REVIEW AND APPROVAL OF ARDEC REPORTS

THIS IS A:

[X] TECHNICAL REPORT   [ ] SPECIAL REPORT

[ ] MEMORANDUM REPORT   [ ] ARMAMENT GRADUATE SCHOOL REPORT

FUNDING SOURCE_____ARDEC S&T_____

[e.g., TEX3; 6.1 (ILIR, FTAS); 6.2; 6.3; PM funded EMD; PM funded Production/ESIP; Other (please identify)]

Wraparound Antenna for S-band Telemetry

Title	Project

Aaron Barton

Author/Project Engineer	Report number/Date received (to be completed by LCSD)

_x3521_   _95_   RDAR-MEF-I

Extension	Building	Author's Office Symbol

PART 1. **Must be signed before the report can be edited.**

  a. The draft copy of this report has been reviewed for technical accuracy and is approved for editing.

  b. Use Distribution Statement A___✓___, B____, C____, D____, E____, or F____ for the reason checked on the continuation of this form. Reason: _____

      1. If Statement A is selected, the report will be released to the National Technical Information Service (NTIS) for sale to the general public. Only unclassified reports whose distribution is not limited or controlled in any way are released to NTIS.

      2. If Statement B, C, D, E, or F is selected, the report will be released to the Defense Technical Information Center (DTIC) which will limit distribution according to the conditions indicated in the statement.

  c. The distribution list for this report has been reviewed for accuracy and completeness.

Craig Sandberg

30 APR 2018

Division Chief	(Date)

PART 2. To be signed either when draft report is submitted or after review of reproduction copy.

This report is approved for publication.

Craig Sandberg   30 July 2020

Division Chief	(Date)

RDAR-CIS	(Date)

LCSD 49 (1 Sept 16)
Supersedes SMCAR Form 49, 20 Dec 06